

A quantitative measure of medium-range order in amorphous materials from transmission electron micrographs

R K Dash¹, P M Voyles², J M Gibson³, M M J Treacy⁴ and P Keblinski¹

¹ Materials Science and Engineering Department, Rensselaer Polytechnic Institute, Troy, NY, USA

² Materials Science and Engineering Department, University of Wisconsin, Madison, WI, USA

³ Advanced Photon Source, Argonne National Laboratory, Argonne, IL, USA

⁴ NEC Research Institute, Princeton, NJ, USA

E-mail: voyles@engr.wisc.edu

Received 20 May 2003

Published 23 July 2003

Online at stacks.iop.org/JPhysCM/15/S2425

Abstract

We propose an extension to the technique of fluctuation electron microscopy that quantitatively measures a medium-range order correlation length in amorphous materials. In both simulated images from computer-generated paracrystalline amorphous silicon models and experimental images of amorphous silicon, we find that the spatial autocorrelation function of dark-field transmission electron micrographs of amorphous materials exhibits a simple exponential decay. The decay length measures a nanometre-scale structural correlation length in the sample, although it also depends on the microscope resolution. We also propose a new interpretation of the fluctuation microscopy image variance in terms of fluctuations in local atomic pair distribution functions.

1. Introduction

Understanding of the properties of amorphous and glassy materials has been hindered by incomplete knowledge of their atomic structure. Until recently, direct experimental data about atomic structure in disordered materials were essentially limited to structure factors $S(k)$ obtained by diffraction [1–3]. The Fourier transform of $S(k)$ yields the pair distribution function, $g_2(r)$, which gives the probability of finding two atoms in the sample separated by a distance r . Although some additional structural information can be inferred from optical, spectroscopic and nuclear magnetic resonance data [4–8], most of the effort in understanding amorphous materials has focused on structural models with a $g_2(r)$ consistent with experiment. The general conclusion of these studies is that model amorphous structures are more or less consistent with that of the continuous random network (CRN) model [9].

However, $g_2(r)$ is not very sensitive to medium-range order (MRO), the ~ 1 nm scale structure present in many amorphous materials. Evidence for MRO comes from the anomalous first sharp diffraction peak found in many ionic and covalent glasses [10] and from small angle scattering [11]. MRO is believed to affect diffusive, mechanical, optical and electronic properties of amorphous materials. For example, the opto-electronic properties of amorphous silicon deteriorate with time [12], which is relevant for solar-cell and flat panel display applications. There is an accompanying change in MRO, but little attendant change in the diffraction spectrum [13–18].

Treacy and Gibson [19] have developed a technique called fluctuation electron microscopy (FEM) to provide more information about MRO in amorphous materials. FEM is the statistical analysis of fluctuations in diffraction from nanometre-scale volumes. Such local diffraction can be measured using a transmission electron microscope (TEM). FEM reveals information based on higher-order atomic distribution functions, which are more sensitive to medium-range structure than $g_2(r)$ [26].

FEM has been used most extensively in studies of amorphous germanium (a-Ge) and silicon (a-Si). The most striking conclusion from these studies is that as-deposited ‘amorphous’ structures contain MRO [20] which is not exhibited by computer-generated CRN models of those materials [21–24]. Instead, the structure of a-Ge and a-Si is better represented by a paracrystalline (PC) model [25]. A PC structure consists of very small, 1–2 nm ordered grains in a CRN matrix. The grains are topologically crystalline, but are strongly strained by the surrounding matrix. This strain, potentially combined with a relatively small grain volume fraction, renders the structure indistinguishable from a CRN by diffraction. The grains, however, cause large local fluctuations in the diffraction from small volumes, so they have a clear FEM signature.

Almost all of the FEM experiments to date have focused on the second moment or variance V of the diffracted intensity distribution. V is systematically measured as a function of the scattering vector magnitude k . (This is described in detail in the next section.) While $V(k)$ is a sensitive probe of the presence and magnitude of MRO, it does not yield a quantitative measure of the characteristic length scale of the ordering, which for a-Si we identify with the PC grain size. This is because the sampling volume of the diffraction measurement is fixed by the size of the TEM point-spread function, or image resolution. It has been shown in simulations [26] and in preliminary experiments [27] that systematic measurements as a function of image resolution can yield an MRO length scale. Unfortunately, these measurements are difficult to make. The resolution of a TEM must be changed mechanically, so a typical TEM can only make measurements at four or five distinct resolutions, which is insufficient data for the previous proposed methods [26].

We propose a different approach to measuring the MRO length scale based on a single-resolution data set. Instead of measuring $V(k)$, we consider the diffracted intensity spatial autocorrelation function $c(r)$. We show in simulations that $c(r)$ has a simple exponential decay form, and that the decay length depends on both the sample structure and the image resolution. Even under unfavourable conditions, measurements at the few discrete resolutions available in most TEMs should serve to extract the sample length scale.

Both $V(k)$ and $c(r)$ address a fundamental difficulty with electron micrographs of amorphous materials: they appear almost completely random to the eye. $V(k)$ measures quantitatively whether an image has larger excursions away from the mean intensity (more or brighter bright pixels, or more or darker dark pixels) than a purely random image. $c(r)$ measures quantitatively whether there are groups of pixels with similar intensity that are larger or occur more often than in a purely random image. The decay length of $c(r)$ is a simple but quantitative measure of the characteristic size of these non-random groupings of pixels.

Fan and Cowley [28] have previously considered the autocorrelation function of high-resolution TEM micrographs as a measure of MRO in amorphous materials. Their analysis focused on finding visual patterns ('fringes') in the two-dimensional autocorrelation function; we focus on quantifying the functional form of the azimuthally averaged autocorrelation. They also worked at only the best resolution available with their TEM. We address the effects of the TEM by systematically studying the effects of the image resolution.

In the next section we provide a theoretical description of the fluctuation microscopy and mathematically define $V(k)$ and $c(r)$ in terms of the sample structure and the microscope imaging conditions. We then describe the autocorrelation function calculated from simulated images of computer-generated structures, which allow us to test our proposed measure of MRO under controlled conditions. Finally, we demonstrate from experimental images that our new analysis generates the same trends as the previous $V(k)$ FEM analysis, but with a greater level of quantification.

2. Theory

The central idea of FEM is to study the statistics of the image intensity. The simplest statistic is the average intensity. The average intensity is simply connected to $S(k)$, so it has little information about MRO. One more complicated statistic is the variance, or the normalized second moment V , defined as

$$V(k, Q) = \frac{\langle I^2(\mathbf{r}, \mathbf{k}, Q) \rangle - \langle I(\mathbf{r}, \mathbf{k}, Q) \rangle^2}{\langle I(\mathbf{r}, \mathbf{k}, Q) \rangle^2} = \frac{\langle I^2(\mathbf{r}, \mathbf{k}, Q) \rangle}{\langle I(\mathbf{r}, \mathbf{k}, Q) \rangle^2} - 1, \quad (1)$$

where $I(\mathbf{r}, \mathbf{k}, Q)$ is the image intensity at point \mathbf{r} , \mathbf{k} is the scattering wavevector, Q controls the microscope resolution and $\langle \rangle$ indicates averaging over \mathbf{r} .

For a thin TEM specimen consisting of a single element imaged at moderate real-space resolution ($\sim 10\text{--}20 \text{ \AA}$) the kinematic coherent dark-field image intensity, $I(\mathbf{r}, \mathbf{k}, Q)$ is proportional to [19]

$$I(\mathbf{r}, \mathbf{k}, Q) \propto \sum_i \sum_j A_i(\mathbf{r}) A_j(\mathbf{r}) \exp(-2\pi \mathbf{k} \cdot \mathbf{r}_{ij}), \quad (2)$$

where \mathbf{r}_{ij} is the vector separating atom i from atom j , and the sums run over all the atoms in the sample. $A_j(\mathbf{r})$ is the point-spread function of the microscope, centred about the position of atom j . $A_j(\mathbf{r})$ is determined by the size and shape of the microscope objective aperture and the objective lens aberrations. For the simplest case of a circular aperture of radius Q and negligible lens aberrations, $A_j(\mathbf{r})$ is the Airy function,

$$A_j(\mathbf{r}) = \frac{J_1[2\pi Q|\mathbf{r} - \mathbf{r}_j|]}{2\pi Q|\mathbf{r} - \mathbf{r}_j|}, \quad (3)$$

where J_1 is the first-order Bessel function. If, instead of using plane wave illumination, we use hollow-cone illumination by averaging over all the in-plane directions of the scattering vector, the image intensity becomes

$$I(\mathbf{r}, k, Q) \propto \sum_j \sum_l A(2\pi Q|\mathbf{r} - \mathbf{r}_j|) A(2\pi Q|\mathbf{r} - \mathbf{r}_l|) J_0(2\pi k|\mathbf{r}_j - \mathbf{r}_l|), \quad (4)$$

where $k = |\mathbf{k}|$ and J_0 is the zeroth-order Bessel function. A detailed derivation of all the imaging equations in consistent notation may be found in [29].

Equation (4) suggests an interpretation of the image intensity as a Fourier transform of a *local* pair distribution function $g_{2A}(r', \mathbf{r}, Q)$ weighted by the Airy function. $g_{2A}(r', \mathbf{r}, Q)$ is defined as

$$g_{2A}(r', \mathbf{r}, Q) = \sum_j \sum_i A(2\pi Q|\mathbf{r} - \mathbf{r}_j|)A(2\pi Q|\mathbf{r} - \mathbf{r}_i|)\delta(|\mathbf{r}_i - \mathbf{r}_j| - r'), \quad (5)$$

where $\delta(r)$ is the Dirac δ -function. Equation (4) can be recovered by integrating $g_{2A}(r', \mathbf{r}, Q)$ times $J_0(2\pi kr')$ over r' , i.e., performing a rotationally invariant Fourier transform in cylindrical coordinates. Normally a distribution function like $g_2(r)$ is an average quantity of the entire sample. Here, contributions to $g_{2A}(r', \mathbf{r}, Q)$ come only from a small volume centred at point \mathbf{r} of size proportional to $1/Q$, the width of the Airy function. If we used a step function instead of an Airy function for the weight, $g_{2A}(r', \mathbf{r}, Q)$ would be exactly a pair distribution function for the cylinder centred at point \mathbf{r} and extending through the thickness of the sample. That would be equivalent to the well known column approximation in electron microscopy [30].

Formulating the image intensity in terms of $g_{2A}(r', \mathbf{r}, Q)$ highlights the difference between $S(k)$ and $V(k)$. $S(k)$ is the Fourier transform of the *spatially averaged* pair distribution function, $g_2(r)$, whereas $V(k)$ measures the magnitude of *spatial variation* between local functions $g_{2A}(r', \mathbf{r}, Q)$. This description also provides another avenue to see the connection between $V(k)$ and higher-order distribution functions, since one way to define higher-order distribution functions is through non-trivial correlations between local pair distributions.

Using $g_{2A}(r')$ also makes calculating $I(\mathbf{r}, k, Q)$ and related quantities such as $V(k, Q)$ much more computationally efficient. The algorithm proceeds as follows: first, $g_{2A}(r', \mathbf{r}, Q)$ is calculated by summing over all the atom pairs within the resolution volume ($\sim 1/Q$) around point \mathbf{r} . Since the resolution volume is finite, this calculation is independent of the model size for a given thickness. Next, $I(\mathbf{r}, k, Q)$ is calculated by one-dimensional numerical integration of $g_{2A}(r', \mathbf{r}, Q) \times J_0(2\pi kr')$ over r' for the desired values of k and Q . Finally, this scheme is repeated at different \mathbf{r} to generate the image, pixel by pixel.

In this paper, we examine the spatial correlations in the image intensity using the autocorrelation function, $c(\mathbf{r})$. We define the normalized $c(\mathbf{r})$ as

$$c(\mathbf{r}) = \frac{\langle [I(\mathbf{r}_1, k, Q) - \langle I(k, Q) \rangle][I(\mathbf{r}_1 + \mathbf{r}, k, Q) - \langle I(k, Q) \rangle] \rangle}{\langle [I(\mathbf{r}_1, k, Q) - \langle I(k, Q) \rangle] \rangle^2}, \quad (6)$$

where $\langle \rangle$ indicates averaging over \mathbf{r}_1 . Further azimuthal averaging can also be performed to yield a one-dimensional $c(r)$, where $r = |\mathbf{r}|$. $c(r)$ is normalized to one at $r = 0$, and goes to zero at large r . Since $c(r)$ depends on I^2 , it, like $V(k)$, depends on the three- and four-atom distribution functions. As we show in the rest of this paper, $c(r)$ distills that information into a form from which we can extract a quantitative MRO correlation length.

3. Simulated images

Simulated images from computer-generated model structures provide a way for us to explore the properties of images from known structures. This has been a primary tool for understanding FEM measurements using $V(k)$ [25, 33], so we turn to it again to help us understand $c(r)$.

We have generated a set of three structural models of PC a-Si using a molecular dynamics synthesis route involving quenching liquid Si in the presence of small crystalline grains using the empirical environment dependent interatomic potential [31]. Details of the synthesis have been given previously [32, 33]. The models have PC grain diameters of 1.3, 1.6 and 1.9 nm, and are labelled Para1, Para2 and Para3. In each case, the grains occupy $\sim 50\%$ of the volume of the model, so the larger grain models contain more atoms. The rest of each model is made

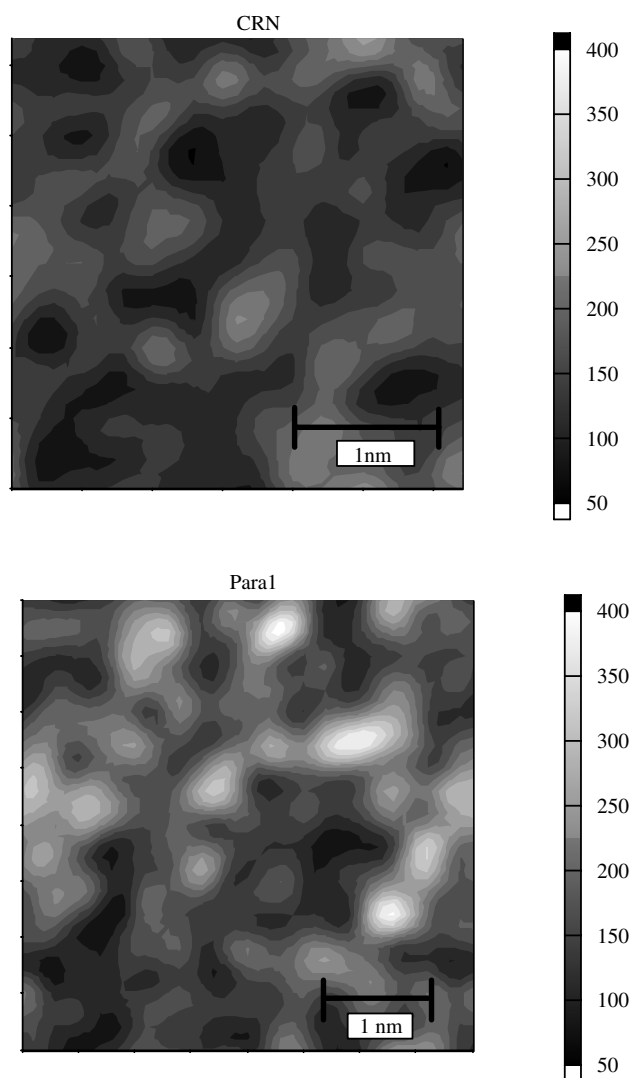


Figure 1. Grey scale contour plots of the calculated image intensity for the CRN and Para1 structures according to equation (4). $Q = 0.056 \text{ \AA}^{-1}$, which is a real-space resolution of $\sim 11 \text{ \AA}$, and $k = 0.56 \text{ \AA}^{-1}$, which is the position of the second maximum in $S(k)$ for a-Si.

up of CRN intergranular material. The earlier models [25, 33] contained only four PC grains and ≤ 1000 atoms, which presented challenges for generalizing to real samples. Our new models contain 64 randomly oriented grains and 8000–16 000 atoms, so they should be more representative. A CRN model with a similar size with no grains was also synthesized for comparison.

Figure 1 shows calculated dark-field images of the CRN and Para1 structures with $k = 0.56 \text{ \AA}^{-1}$ and $Q = 0.056 \text{ \AA}^{-1}$ (real-space resolution of 11 \AA). The value of k corresponds to the second peak in the structure factor for amorphous Si. The images were calculated on a square mesh with a mesh size of $a_0/2$, where $a_0 = 5.43 \text{ \AA}$ is the lattice parameter of crystalline Si. These images were calculated using equations (3)–(5) with a cut-off distance for the local

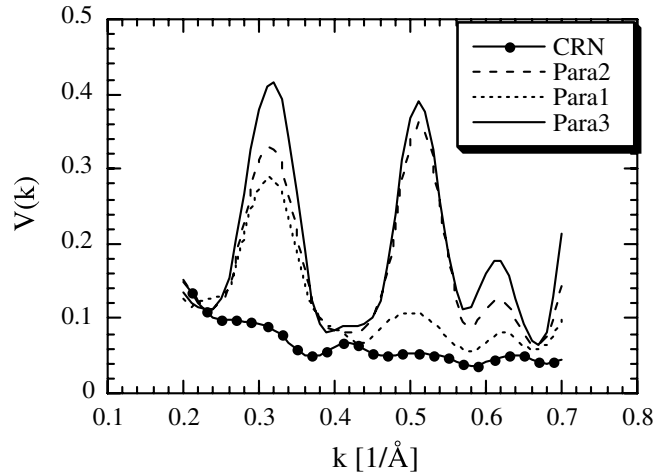


Figure 2. $V(k)$, the standard FEM signal, calculated at $Q = 0.056 \text{ \AA}^{-1}$ for all the structures.

pair distribution functions, $g_{2A}(r')$, equal to $0.61/Q \approx 11 \text{ \AA}$, which is the position of the first zero of the Airy function. Using a larger cut-off does not significantly change the results.

These images are in good agreement with images calculated with standard EM simulation packages, e.g. *autoslice* by Kirkland [34], which is a full dynamical scattering simulation using a plane-wave multislice algorithm. This has two important consequences. First, it means that the assumptions that go into equation (4), namely kinematic scattering and negligible lens aberrations, are very good, at least at the small thickness of the models. In a zone-axis oriented crystal, dynamical scattering becomes important in only a few nanometres [35]. Second, the code based on equation (4) is much faster than the full dynamical treatment, which makes it computationally feasible to screen large portions of the model configuration and imaging parameter phase spaces simultaneously.

The images in figure 1 are displayed on the same grey scale to make it clear that the Para1 image exhibits larger intensity fluctuations than the CRN image. These fluctuations are quantified in figure 2, which shows $V(k)$ for all the models. $V(k)$ for the CRN is small, and essentially featureless. $V(k)$ for Para1 is larger, and shows two clear peaks at $k = 0.31$ and 0.56 \AA^{-1} . The magnitude of these peaks increases with increasing MRO, as noted previously [25, 33]. The structure factor $S(k)$ of the models (not shown) displays only small changes from the CRN to Para2. Para3 shows some splitting of the second peak, which is an experimental indicator of crystallinity.

Now we turn our attention to the intensity autocorrelation function, $c(r)$. Figure 3(a) shows $c(r)$ calculated using equation (6) for all the model structures with $Q = 0.056 \text{ \AA}^{-1}$ and $k = 0.56 \text{ \AA}^{-1}$. In all cases $c(r = 0) = 1$, and $c(r)$ decays to zero for large r . However, the decay rate is fastest for the CRN and decreases with increasing MRO. This is even more apparent on the log-normal plot shown in figure 3(b). In the 5–10 \AA range all $c(r)$ functions are well fitted by an exponential decay,

$$c(r) = \exp(-r/\lambda), \quad (7)$$

where λ is the decay length. λ is the smallest for the CRN structure, and increases as the size of PC grains increases.

We also calculated $c(r)$ at $k = 0.31 \text{ \AA}^{-1}$, the position of the first peak in $S(k)$ (as well as $V(k)$), for the CRN and Para1 structures. As shown in figure 4, the correlation functions and

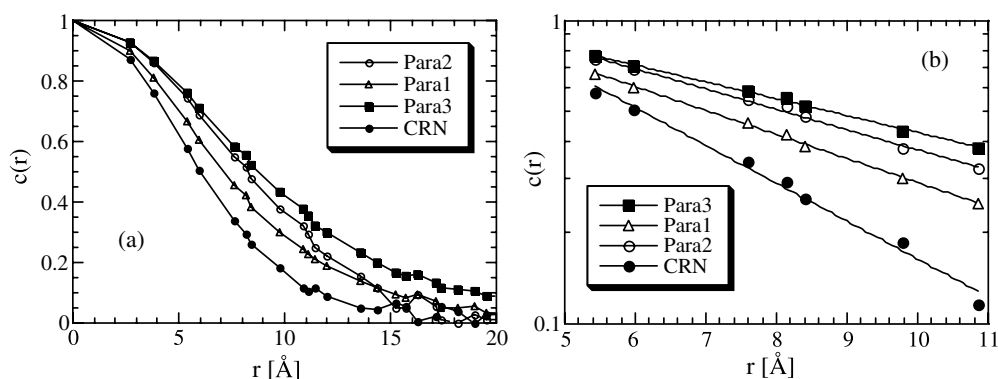


Figure 3. The intensity autocorrelation functions, $c(r)$ calculated for the simulated images of the four model structures. $Q = 0.056 \text{ \AA}^{-1}$ and $k = 0.56 \text{ \AA}^{-1}$. (a) linear scale, (b) log-linear scale.

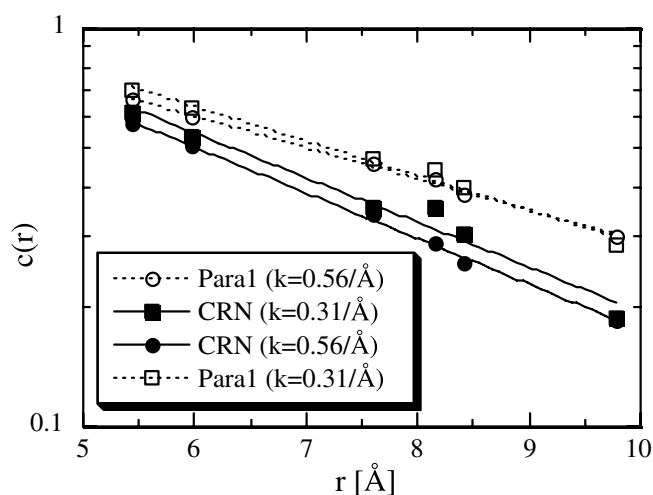


Figure 4. The intensity autocorrelation functions, $c(r)$, for CRN and Para1 structures calculated at $k = 0.31$ and 0.56 \AA^{-1} , i.e., the position of the first and the second maximum in $S(k)$ for a-Si. The correlation lengths λ are relatively insensitive to k .

correlation lengths calculated for $k = 0.31$ and 0.56 \AA^{-1} are essentially the same. We take this as evidence that λ is sensitive primarily to the size of the PC grains, not the details of the imaging conditions.

Figure 5(a) explicitly shows this correlation by graphing λ calculated at $k = 0.56 \text{ \AA}^{-1}$ as a function of d , the size of the crystalline grains introduced into the models during synthesis. d is correlated with many other topological, real-space and experimental measures of MRO [33]. For $Q = 0.11 \text{ \AA}^{-1}$ (5.5 \AA real-space resolution), λ is approximately equal to $1/3d$. For $Q = 0.055 \text{ \AA}^{-1}$ (11 \AA real-space resolution), λ shows a weaker but still monotonic trend with d .

The effects of microscope resolution are shown in figure 5(b). λ systematically increases with increasing real-space resolution. At large resolution $\geq 15 \text{ \AA}$ λ becomes more or less proportional to the resolution. However, at small resolution, $\leq 5 \text{ \AA}$, the value of the correlation length becomes essentially resolution independent. It remains, however, correlated with the structure: at small resolution, λ increases with the increasing PC grain size in the model. This

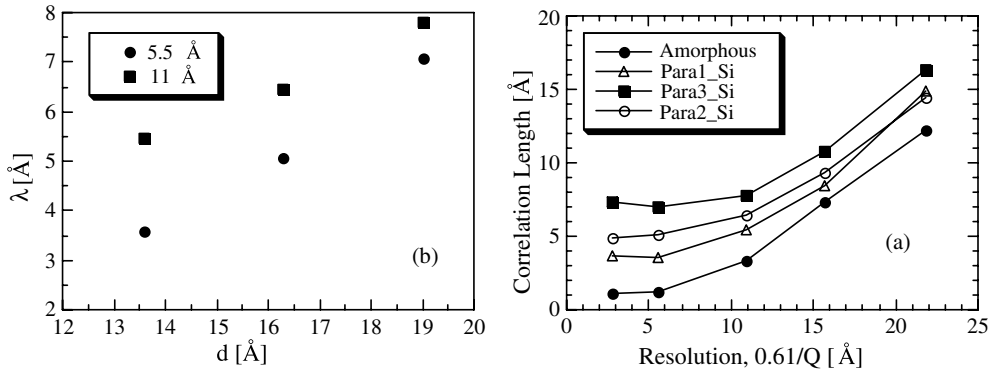


Figure 5. (a) The correlation length λ as a function of the size of the grains introduced into the model, d , at 5.5 and 11 Å real-space resolution and $k = 0.56 \text{ \AA}^{-1}$. λ increases with d in both cases, indicating correlation between λ and a known length scale in the model. (b) The correlation length λ as a function of the real-space microscope resolution. At small resolution, λ is independent of the resolution. At large resolution, λ depends on the sample structure and the resolution.

indicates that λ at small real-space resolutions directly measures the extent of the paracrystal size. For resolutions $\leq 2 \text{ \AA}$, the assumption of negligible lens aberrations start to break down, but for a modern TEM it should still be valid for a resolution of 5 Å.

4. Experimental images

We have calculated the autocorrelation function from hollow-cone dark-field images of a series of a-Si samples deposited at increasing substrate temperature. Samples were deposited by magnetron sputtering on rock salt at a substrate temperature T_s of 200, 250, 300 and 350 °C to a nominal thickness of 200 Å. Images were acquired on a Hitachi H9000 TEM at 200 kV using an objective aperture with $Q = 0.04 \text{ \AA}^{-1}$, which corresponds to a real-space resolution of $\sim 15 \text{ \AA}$. $c(r)$ was calculated from images at $k = 0.55 \text{ \AA}^{-1}$. We first azimuthally averaged the $c(r)$ from each image, then averaged the $c(r)$ from ten images of the same sample. The error bars are one standard deviation of the mean from the ten images. More details on the sample preparation and imaging can be found in [37].

$c(r)$ for these samples is reasonably well fitted by an exponential decay, as shown in figure 6 for $T_s = 200$ and 350 °C. The straight lines are exponential fits to the data over the range indicated. The small- r limit of the fit window was fixed at $r = 2.34 \text{ \AA}$ to avoid the short-range decay determined by large-scale structure in the sample. The large- r limit of the fit window was selected independently for each sample to give a linear correlation coefficient $R \geq 0.9$. For the lowest $T_s = 200 \text{ °C}$, which is the best fit, this results in a fit from $r = 2.34$ to 11.12 Å, which is 17 data points. For the worst case, $T_s = 300 \text{ °C}$, the fit is from $r = 2.34$ to 5.85 Å, which is six data points.

The match to an exponential form in both simulated images from atomistic models and in experimental data may tell us something important about the underlying PC structure. Previous detailed analysis of the structure of smaller PC atomistic models has suggested that the PC grains do not have a sharp interface with the amorphous matrix [32, 33]. Rather, they have more ordered core, and the structural order decreases with distance from that core. The models discussed here have the same property and an exponential $c(r)$. A simple model of a structure

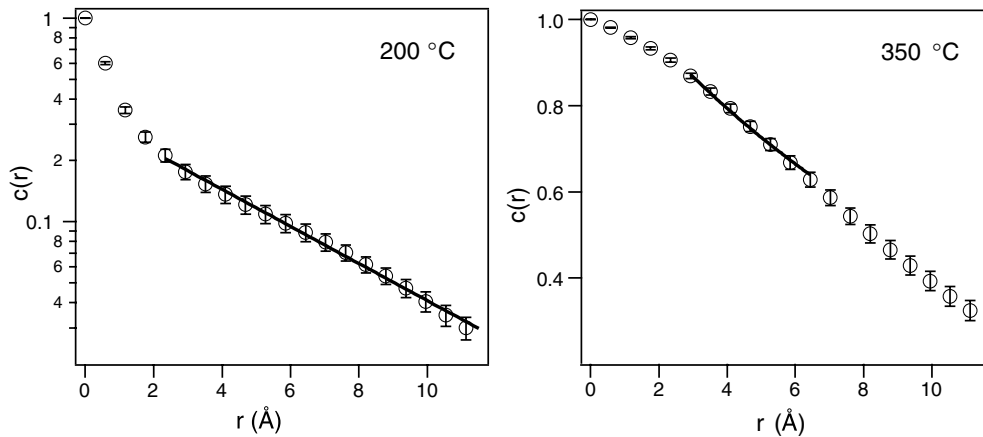


Figure 6. Experimental $c(r)$ from dark-field images of a-Si deposited on substrates held at $T_s = 200$ and 350 °C. The straight lines are exponential decays fit to the data over the range indicated. The fitting range is selected to yield a linear correlation coefficient $R \geq 0.9$. The poorer fit at higher T_s is due to the large scale morphology of the sample.

with sharp interfaces, consisting of randomly placed overlapping spheres and some stochastic noise does not produce an exponential form for $c(r)$; instead $c(r)$ decays more steeply to zero near the diameter of the spheres. This suggests that the low- T_s experimental samples may also have diffuse PC grain/amorphous matrix interfaces, while the higher- T_s samples may have somewhat sharper interfaces.

However, the increasingly poor fit at large T_s is probably also strongly influenced by the increasing tendency of the films to develop a beadlike morphology at a length scale of ~ 350 Å. This is not MRO, but simply a result of poor wetting of Si on the NaCl substrate. $c(r)$ for a random distribution of spheres is not an exponential, especially at larger r , so as this structure becomes more apparent, the deviation of the experimental $c(r)$ from an exponential form grows. Methods have been developed to correct $V(k)$ for this kind of structure [36]; similar corrections will also need to be developed in the future for this new analysis.

Previous experiments in which $V(k)$ was calculated from the same set of images indicated that the degree of MRO increases monotonically with increasing T_s [37]. Figure 7 shows that the same trend holds true in the decay length λ as a function of T_s . Over the range $T_s = 200$ to 350 °C, the electron structure factor barely changes [37]. This is evidence that λ from $c(r)$ is measuring similar MRO to $V(k)$, but in a more quantitative way. To fully quantify these observations would require measuring λ at several microscope resolutions, which has not yet been done.

5. Summary

We propose a new quantitative measure of MRO in amorphous materials, related to the technique of FEM. The spatial autocorrelation function of the dark-field TEM image intensity is found to exhibit an exponential decay. The decay length is determined by an intrinsic structural correlation length and the microscope resolution. Our analysis indicates that measurements at a few discrete resolutions are sufficient to separate these effects and determine the intrinsic correlation length. We have demonstrated this measure of MRO in simulated images from computer-generated models of a-Si and in experimental images of a-Si. The correlation length

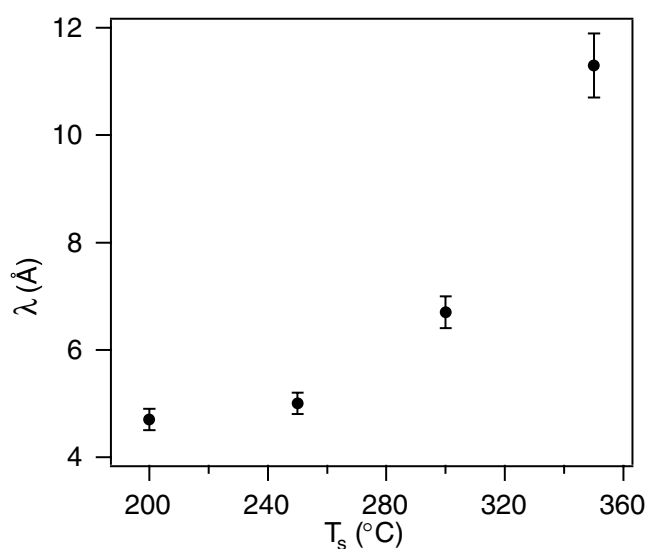


Figure 7. Correlation length λ extracted from the autocorrelation function $c(r)$ as a function of substrate temperature during deposition T_s . These data show the same trend towards increasing MRO with increasing T_s as previously observed [37].

from the simulations follows the degree of medium-range order introduced *a priori* into the models. The correlation length in the experiment shows the same trend as previous FEM measurements on the same samples.

A great deal of work remains to fully understand the properties of the autocorrelation function and its decay length. Connections could be made analytically with three- and four-body atom distribution functions, and hopefully with other aspects of the sample structure such as a PC grain size or the bonding topology. Experimentally, we must find ways to deal with variations in sample thickness and morphology which can affect the measured correlation length and determine the number of measurements that must be made at different resolutions to fully remove the effects of the microscope. Once this work is completed, we will have a powerful new tool to quantitatively characterize medium-range order in amorphous materials.

Acknowledgments

We thank Dr J E Gerbi and Dr J R Abelson for the amorphous silicon samples. RD and PK acknowledge the support of the National Science Foundation under grant no DMR 00-74273.

References

- [1] Moss S C and Graczyk J F 1969 *Phys. Rev. Lett.* **23** 1167–71
- [2] Etherington G *et al* 1982 *J. Non-Cryst. Solids* **48** 265–89
- [3] Temkin R J, Paul W and Connel G A N 1974 *Adv. Phys.* **22** 581–641
- [4] Elliot S R 1989 *Adv. Phys.* **38** 1–88
- [5] Beeman D, Tsu R and Thorpe M F 1985 *Phys. Rev. B* **32** 874–8
- [6] Maley N, Beeman D and Lannin J S 1988 *Phys. Rev. B* **38** 10611–22
- [7] Sokolov A P and Shebanin A P 1990 *Sov. Phys.–Semicond.* **24** 720–2
- [8] Langford A A, Fleet M L, Nelson B P, Langford W A and Maley N 1992 *Phys. Rev. B* **45** 13367–77
- [9] Zachariasen W H 1932 *J. Am. Chem. Soc.* **54** 3841

- [10] Moss S C and Price D L 1985 *Physics of Disordered Materials* ed A Adler, H Fritzsche and S R Ovshinsky (New York: Plenum) pp 77–95
- [11] Williamson D L 1994 *Amorphous and Microcrystalline Silicon Technology (Mater. Res. Soc. Symp. Proc. vol 377)* (Pittsburgh, PA: Materials Research Society) pp 251–62
- [12] Staebler D L and Wronski C R 1977 *Appl. Phys. Lett.* **31** 292–4
- [13] Gibson J M, Treacy M M J, Voyles P M, Jin H-C and Abelson J R 1998 *Appl. Phys. Lett.* **73** 3093–5
- [14] Fritzsche H 1997 *Amorphous and Microcrystalline Silicon Technology* pp 19–30
- [15] Masson D P, Ouhlal A and Yelon A 1995 *J. Non-Cryst. Solids* **190** 151–6
- [16] Fan J and Kakalios J 1994 *Phil. Mag. B* **69** 595–608
- [17] Norberg R E *et al* 1991 *Amorphous and Microcrystalline Silicon Technology (Mater. Res. Soc. Symp. Proc. vol 25)* (Pittsburgh, PA: Materials Research Society) pp 377–82
- [18] Gotoh T, Nonomura S, Nishio M, Nitta S, Kondo M and Matsuda A 1998 *Appl. Phys. Lett.* **72** 2978–80
- [19] Treacy M M J and Gibson J M 1996 *Acta Crystallogr. A* **52** 212–20
- [20] Gibson J M and Treacy M M J 1997 *Phys. Rev. Lett.* **78** 1074–7
- [21] Wooten F, Winer K and Weaire D 1985 *Phys. Rev. Lett.* **54** 1392–5
- [22] Ding K and Andersen H C 1986 *Phys. Rev. B* **10** 6987–90
- [23] Kelires P C and Tersoff J 1988 *Phys. Rev. Lett.* **61** 562–5
- [24] Luedtke W D and Landman U 1989 *Phys. Rev. B* **40** 1164–74
- [25] Treacy M M J, Gibson J M and Keblinski P J 1998 *J. Non-Cryst. Solids* **231** 99–110
- [26] Gibson J M, Treacy M M J and Voyles P M 2000 *Ultramicroscopy* **83** 169
- [27] Voyles P M and Muller D A 2002 *Ultramicroscopy* **93** 147
- [28] Fan G Y and Cowley J M 1985 *Ultramicroscopy* **17** 345
- [29] Voyles P M 2001 *PhD Dissertation* University of Illinois at Urbana-Champaign, Department of Physics
- [30] Hirsch P, Howie A, Nicholson R, Pashley W and Whelan M J 1977 *Electron Microscopy of Thin Crystals* (Malabar, FL: Krieger) p 156
- [31] Justo J F *et al* 1998 *Phys. Rev. B* **58** 2539–50
- [32] Keblinski P, Phillpot S R, Wolf D and Gleiter H 1997 *Acta Mater.* **45** 987–98
- [33] Voyles P M, Zotov N, Nakhmanson S M, Drabold D A, Gibson J M, Treacy M M J and Keblinski P J 2001 *J. Appl. Phys.* **90** 4437
- [34] Kirkland E J 1998 *Advanced Computing in Electron Microscopy* (New York: Plenum)
- [35] Fertig J and Rose H 1981 *Optik* **59** 407–29
- [36] Voyles P M, Treacy M M J, Gibson J M, Jin H-C and Abelson J R 2001 *Advances in Materials Problem Solving with the Electron Microscope (Mater. Res. Soc. Symp. Proc. vol 589)* ed J Bentley *et al* (Pittsburgh, PA: Materials Research Society) p 155
- [37] Voyles P M, Gerbi J E, Treacy M M J, Gibson J M and Abelson J R 2001 *Phys. Rev. Lett.* **86** 5514–18